Biophysical Journal Volume 74 May 1998 2210–2222

Temporally and Spectrally Resolved Imaging Microscopy of Lanthanide Chelates

György Vereb,*[#] Elizabeth Jares-Erijman,*[§] Paul R. Selvin,[¶] and Thomas M. Jovin*

*Department of Molecular Biology, Max Planck Institute for Biophysical Chemistry, D-37070 Göttingen, Germany; [#]Department of Biophysics and Cell Biology, University Medical School of Debrecen, 4012 Debrecen, Hungary; [§]Department of Organic Chemistry, University of Buenos Aires, 1428 Buenos Aires, Argentina; and [¶]Department of Physics, University of Illinois at Urbana-Champaign, Urbana, Illinois 61801 USA

ABSTRACT The combination of temporal and spectral resolution in fluorescence microscopy based on long-lived luminescent labels offers a dramatic increase in contrast and probe selectivity due to the suppression of scattered light and short-lived autofluorescence. We describe various configurations of a fluorescence microscope integrating spectral and microsecond temporal resolution with conventional digital imaging based on CCD cameras. The high-power, broad spectral distribution and microsecond time resolution provided by microsecond xenon flashlamps offers increased luminosity with recently developed fluorophores with lifetimes in the submicrosecond to microsecond range. On the detection side, a gated microchannel plate intensifier provides the required time resolution and amplification of the signal. Spectral resolution is achieved with a dual grating stigmatic spectrograph and has been applied to the analysis of luminescent markers of cytochemical specimens in situ and of very small volume elements in microchambers. The additional introduction of polarization optics enables the determination of emission polarization; this parameter reflects molecular orientation and rotational mobility and, consequently, the nature of the microenvironment. The dual spectral and temporal resolution modes of acquisition complemented by a posteriori image analysis gated on the spatial, spectral, and temporal dimensions lead to a very flexible and versatile tool. We have used a newly developed lanthanide chelate, Eu-DTPA-cs124, to demonstrate these capabilities. Such compounds are good labels for time-resolved imaging microscopy and for the estimation of molecular proximity in the microscope by fluorescence (luminescence) resonance energy transfer and of molecular rotation via fluorescence depolarization. We describe the spectral distribution, polarization states, and excited-state lifetimes of the lanthanide chelate crystals imaged in the microscope.

INTRODUCTION

Long-lived luminescent labels are being applied increasingly in fluorescence microscopy. Time-gated detection permits the efficient suppression of scattered light and short-lived autofluorescence from cytochemical samples and optical components (Beverloo et al., 1992; Hennink et al., 1996; Jovin et al., 1990; Marriott et al., 1991, 1994; Verwoerd et al., 1994). These methods are based on intermittent (pulsed) or periodic (modulated) excitation and detection windows displaced in time or phase with respect to the excitation. The simplest implementation of intermittent excitation is via a chopper wheel placed in the conventional excitation path of the fluorescent microscope with the aid of proper focusing elements. This modification is relatively easy to introduce and is cost effective. However, although proper focusing of the beam can provide timing with a resolution of $\sim$50 μs (Marriott et al., 1991), the minimal illumination window is limited to some hundreds of microseconds. This excludes the use of shorter-lived probes offering the potential of higher luminosity, as deactivation during illumination periods longer than the excited-state lifetime leads to a reduced steady-state rate of emission. Furthermore, the inherent kinetics of the chemical and biochemical processes under observation may dictate observation in the submillisecond range. Acousto-optical modulators (AOMs) and electro-optical modulators (EOMs) offer faster timing (nano- to milliseconds), but their use is generally restricted to highly collimated illumination sources such as lasers. The recently introduced liquid crystal and ferroelectric shutters provide intermediate temporal performance (Verwoerd et al., 1994) and large apertures.

Recently improved pulsed sources (lasers and flashlamps) constitute alternative solutions. For example, N_2 lasers deliver pulses in the 0.5–5 ns range with millijoule energies. Numerous laser dyes provide excitation wavelengths between 350 and 750 nm (or higher into the near infrared region). An alternative to pulsed lasers are nanosecond flashlamps. These sources are incoherent and generally achieve higher repetition rates (100 Hz up to several kHz) depending upon the electrode separation and filling gas. The latter also determines the spectral properties of emitted light, which can be dominated by lines (e.g., in the case of deuterium, nitrogen, and argon) or be quasi-continuous (e.g., with xenon), in which case the appropriate band(s) may be selected by filters or a monochromator. The full width at half maximum (FWHM) of the pulse extends over a wide range (submicrosecond to millisecond depending on the storage capacitor), permitting the determination

---

Received for publication 29 October 1997 and in final form 31 December 1997.

Address reprint requests to Dr. Thomas M. Jovin, Department of Molecular Biology, Max Planck Institute for Biophysical Chemistry, Am Fassberg, D-37077 Göttingen, Germany. Tel.: 49-551-2011381; Fax: 49-551-2011467; E-mail: tjovin@mpc186.mpibpc.gwdg.de.

0006-3495/98/05/2210/13 $2.00

of decay processes in the 0.1 μs to 10 ms range. Thus, for detecting luminescence from long-lived probes, a microsecond flash provides efficient excitation in a fraction of the luminescence lifetime. Such microsecond xenon flashlamps have become available commercially; one such unit features pulses of up to 0.1 J at a repetition rate of up to 200 Hz. Its broad spectral range makes it ideal for microspectroscopic imaging applications.

There are also multiple strategies for time-resolved detection. Fast electronic shutters or choppers placed in the emission path (Marriott et al., 1991) allow timing in the 0.1–1 ms range, but the exposure time is not uniform throughout the field of illumination. Liquid crystal and ferroelectric shutters are faster and allow spatially uniform timing, but their transmission and contrast ratio are often insufficient; thus, they are sometimes used in tandem (Verwoerd et al., 1994). Pockels cell shutters are very fast but have a limited repetition rate and optical aperture. Gateable intensifiers, particularly of the microchannel plate (MCP) design, can be gated and modulated at high speed and provide additional gain. They are thus useful for time-resolved (boxcar detection) or frequency/phase-resolved imaging (Clegg et al., 1994; Gadella et al., 1994, 1993; Gadella and Jovin, 1995; Konig et al., 1996; Lakowicz et al., 1994). Their primary limitations are related to cost and deterioration of spatial resolution.

Lanthanide chelates are luminescent compounds with lifetimes on the order of 10–2000 μs. These long-lived probes are better suited for time-resolved microscopy than compounds emitting from the triplet state because they have a high quantum yield and are generally insensitive to oxygen. They have been successfully employed in immunocytochemistry (Seveus et al., 1992), in situ hybridization (Dahlen et al., 1994; de Haas et al., 1996; Seveus et al., 1992), and gene analysis (Kwiatkowski et al., 1994). Time-resolved fluoroimmunoassays employing lanthanide chelates as labels have also been developed for in vitro diagnostics (Altamirano-Bustamante et al., 1991; Barnard et al., 1989; Ci et al., 1995; for a review see Dickson et al., 1995). An active and parallel development of long-lived probes has emphasized other metal ligand complexes, e.g., of the porphyrin family of heterocycles, and multidentate liganded osmium and ruthenium (Hennink et al., 1996; Terpetschnig et al., 1995b; Youn et al., 1995).

Fluorescence resonance energy transfer (FRET) between lanthanide ions and tryptophan residues of enzymes or other luminescent labels bound to proteins has been extensively used in studying the conformation of molecules (Burroughs et al., 1994; Churchich, 1995; Clark et al., 1993; Joshi and Shamboo, 1988; Kwok and Churchich, 1994; Martini et al., 1993; Walters and Johnson, 1990). Recently, certain lanthanide chelates have been used as donors in intermolecular luminescence resonance energy transfer measurements (LRET) (Heyduk and Heyduk, 1997; Mathis, 1995; Root, 1997; Selvin and Hearst, 1994; Selvin et al., 1994). The unique potential of these chelates as luminescent donors for LRET derives from 1) sharp emission peaks, 2) generally high quantum yields, 3) long lifetimes, and 4) generally unpolarized emission (but see below) (Selvin, 1995). In addition, they have large (>150 nm) Stokes shifts and good solubility. The long lifetime, when exploited by time-resolved detection, provides the means for excluding the contribution of short-lived acceptor fluorescence arising from direct excitation. Thus, the donor characteristics can be assessed accurately for the estimation of the FRET efficiency.

Although the characteristic emission lines and large Stokes shift by themselves lead to efficient background suppression using appropriate filters, a spectrally resolved system can provide further selectivity and discrimination in detection, particularly when coupled to an imaging system. We describe here what to our knowledge is the first implementation of combined spatial, spectral, temporal, and polarization resolution in a fluorescence microscope using the emission of lanthanide probes. The measurements were carried out with a system incorporating a chopped arc lamp or a microsecond flashlamp. Detection was with an astigmatism-corrected imaging spectrograph coupled to a gated MCP image intensifier and a slow-scan CCD camera.

MATERIALS AND METHODS

Preparation of Eu-DTPA-cs124 crystals

Eu-DTPA-cs124 crystals (Fig. 1) were used in all experiments. The synthesis (Li and Selvin, 1995), crystallization procedure, and atomic structure have been described (Selvin et al., 1996). Crystals were pipetted from their saturated solution onto a glass slide, briefly rinsed with water, and sealed under a quartz coverslip.

Time-resolved luminescence imaging microscopy

For time-resolved detection, the excitation beam from a 100-W Hg lamp was focused onto a light beam chopper (model 221, HMS Electronic, Ithaca, NY). The recollimated beam was coupled into a Zeiss Axioplan microscope via the standard epifluorescent pathway, incorporating an Omega Optical (Brattleboro, VT) 340DF11 excitation bandpass filter and a Zeiss FT395 dichroic mirror and LP400 longpass emission filter. A trigger TTL pulse from a photodiode was fed into a delay/pulse generator (model DG535, Stanford Research Instruments, Palo Alto, CA), which gated the photocathode of the intensified relay optics (IRO, PCO Computer Optics, Kelheim, Germany) on the detection side. The light emitted from the P43 phosphor was relayed through an *f*/1.2 Nikon lens onto the Kodak KAF-1400 chip of a Photometrics (Tucson, AZ) series 200 cooled slow-scan CCD camera, interfaced to a Macintosh Quadra 800 computer (Apple Computer, Cupertino, CA). Images were collected throughout several (500–1000) excitation-emission cycles and digitized with 12-bit resolution. Conventional microscopic images were taken with the same camera after removing the intensifier.

In other experiments, a microsecond xenon flashlamp (model 5000XeF, IBH Consultants, Glasgow, UK) was used for excitation. The output light was collimated and passed through a liquid filter for IR protection and an Omega 330WB80 wideband UV filter. The refocused beam was coupled into the microscope with a custom-built filter holder replacing the standard Zeiss filter block (see below). Omega 400DCLP02 and 400EFLP were used as the dichroic and emission filters, respectively. All lenses in the excitation light path were made of quartz. The rising edge of the flash was used to trigger the delay/pulse generator. A Zeiss Ultrafluar glycerol immersion objective (40×, NA 0.6) was used for all measurements.

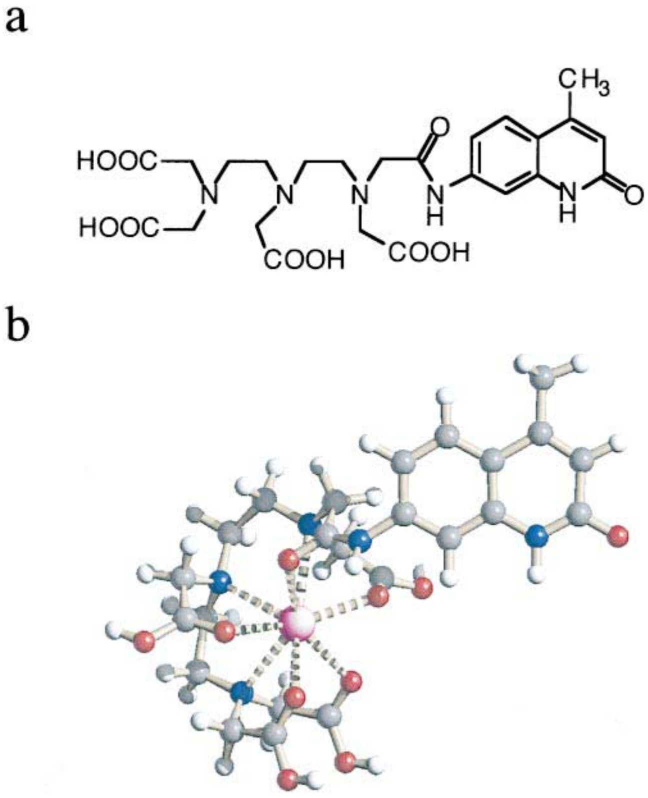

FIGURE 1 The chemical structure and three-dimensional molecular model of DTPA-cs124. (*a*) Chemical structure of DTPA-cs124. (*b*) Molecular model of DTPA-cs124 with a chelated Eu^{3+} ion. The structure was built in Sybyl 6.3 based on crystallographic data from Selvin et al. (1996). The image was generated with the Schakal92 program. Only one complex is represented, although the asymmetric unit cell is composed of two molecules of Eu-DTPA-cs124. The Eu-Eu distance is 9.9 Å and the cs124-cs124 distance is 3.39 Å, showing large π-stacking.

Spectrally resolved luminescence imaging microscopy

Spectral imaging was done with a SpectraPro-150 dual grating stigmatic imaging spectrograph (Acton Research Corp., Acton, MA) occupying the second camera port of the Zeiss Axioplan microscope. The data were obtained with a 300 grooves/mm ruled grating or a 1200 grooves/mm holographic grating having 5 nm/mm and 20 nm/mm nominal dispersions, respectively. Images without spectral resolution were taken with the input slit opened to 3 mm and the grating set to 0 nm central wavelength (nondispersive, or imaging, mode). Spectra were taken at 50 or 100 μm slitwidth and various central wavelengths using spectral images acquired with 16-bit resolution. An SBIG (Santa Barbara Instruments Group, Santa Barbara, CA) ST-6 cooled imaging CCD camera was used. The original vertical spatial information of the imaged strip constituted one dimension, and the corresponding spectra constituted the other. A 1×2 or 3×2 binning was used on the 750×242 (23×27 μm) pixel chip, which was chilled thermoelectrically to -30°C. Spectra were calibrated using defined mercury lines and processed with the KestrelSpec program (RHEA Corp., Wilmington, DE).

Epi-illumination was provided by a 50-W mercury arc lamp or, in the case of time-resolved measurements, the IBH model 5000XeF microsecond flashlamp. A Zeiss Ultrafluar glycerol immersion objective (40×, NA 0.6) was used in combination with an Omega XF02 filter set (330WB80 excitation, 400DCLP02 dichroic, and 400EFLP emission).

Combined time- and spectrum-resolved luminescence imaging microscopy

For achieving temporal and spectral resolution simultaneously, the gated intensifier was adapted to the exit port of the imaging spectrograph. The SBIG CCD camera was mounted onto the intensifier and used to integrate several excitation-delayed emission cycles. Spectral and spatial information was contained in the two-dimensional image of the CCD; temporal resolution was implemented in a boxcar mode by varying the delay between excitation and detection and the open time of the photocathode.

Polarization measurements

The polarization of europium emission was measured in the spectrally resolved imaging mode using a 300 grooves/mm grating. A polarizer and an analyzer on rotating mounts were introduced into the epifluorescence excitation and emission paths, respectively. The optical axes for excitation and emission were coincident and oriented along the top-to-bottom axis. The polarization state oriented left to right when facing the microscope was defined as horizontal and that orthogonal to it as vertical. Spectral images were taken with both horizontal and vertical positioning of the polarizer (${}_{h}I$ and ${}_{v}I$, respectively) and the analyzer set parallel (${}_{h}I_{h}$ and ${}_{v}I_{v}$) and perpendicular (${}_{h}I_{v}$ and ${}_{v}I_{h}$) to the polarizer. The polarization values P_{h} and P_{v} were defined as

$$P_{h} = ({}_{h}I_{h} - G_{h}\,{}_{h}I_{v})/({}_{h}I_{h} + G_{h}\,{}_{h}I_{v}) \tag{1}$$

and

$$P_{v} = ({}_{v}I_{v} - G_{v}\,{}_{v}I_{h})/({}_{v}I_{v} + G_{v}\,{}_{v}I_{h}), \tag{2}$$

where

$$G_{h} = {}_{h}I_{h}/{}_{h}I_{v} \quad \text{and} \quad G_{v} = {}_{v}I_{v}/{}_{v}I_{h} \tag{3}$$

are the usual correction factors for vertical and horizontal polarizer positions measured using a solution with zero anisotropy as in the approach described in Dix and Verkman (1990).

Image processing

Time-resolved image sequences were imported into SCIL-Image (TPD, University of Delft, Delft, The Netherlands) run on an SGI Indy computer (Silicon Graphics, Mountain View, CA). Pixel-by-pixel single-exponential fitting of luminescence decay times was performed using the program DECAY (Gadella and Jovin, 1995, 1997). Other image processing tasks were carried out with SCIL-Image and National Institutes of Health-Image (National Institutes of Health, Bethesda, MD). The molecular structure was generated with Sybyl 6.3 (Tripos, St. Louis, MO) and visualized with the Schakal92 program of E. Keller.

RESULTS AND DISCUSSION

Molecular structure of the Eu-DTPA-cs124

Fig. 1 *a* shows the chemical structure of DTPA-cs124 and Fig. 1 *b* the molecular model based on the crystal structure (Selvin et al., 1996) of DTPA-cs124 with a chelated Eu^{3+} ion. The europium ion is coordinated by nine ligands, consisting of three amines, four carboxylate oxygen atoms, one amide oxygen from the linkage between DTPA and cs124, and one amide oxygen from the carbostyril of the second half of the dimer comprising the unit cell. The environment around the europium is highly asymmetrical. Based on the diminished lifetime in the crystal as compared with that in D_2O (Selvin et al., 1996), it has been suggested that the symmetry surrounding the europium is more anisotropic in the crystal state than in solution.

Microscope imaging system with spectral and temporal resolution

Temporally and spectrally resolved imaging microscopy was performed on a Zeiss Axioplan upright microscope with dual camera ports. A schematic diagram of the system built around the microscope is presented in Fig. 2. The major additions to the standard features of the microscope were the capabilities for intermittent excitation, gated detection, and imaging through a spectrograph.

For intermittent excitation, two approaches were used. In one, a chopper wheel with dual adjustable slits was interposed into the regular epifluorescence excitation light path. This required the refocusing of the beam onto the plane of the chopper and subsequent recollimation. The chopper was operated at 100 Hz, and the slits were adjusted to produce 1-ms illumination periods interspersed by 4-ms dark intervals. The trigger signal for gating the detection was derived from a photodiode built into the chopper.

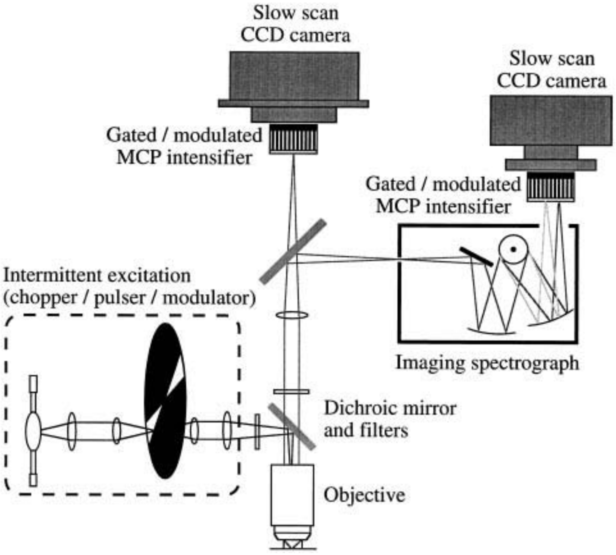

FIGURE 2 Schematics of the generic time-resolved and spectrally resolved imaging microscope system. The depicted light source is a mercury pressure lamp with a DC power supply; the emitted light is focused, chopped with a rotating wheel, and coupled into the conventional epifluorescence excitation path of a microscope. Alternatively, pulsed or modulated light sources can be used for intermittent excitation and can also be coupled directly to the filter block using a custom design. The filter block comprises the classical elements: excitation filter, dichroic mirror, and emission filter, selected according to the fluorophores used. In the system presented, a dual emission port is used, allowing for the concurrent installation and alignment/focusing of both a time-resolved and a spectrally resolved detection system. The time-resolved system in our case comprises a gated, modulated microchannel plate (MCP) intensifier and a cooled slow-scan charge-coupled device (CCD) camera. The other emission port is used to host a stigmatic imaging spectrograph. Detection is also with a cooled slow-scan CCD camera. Optionally, the gated MCP intensifier can be mounted on the spectrograph to extend spectral resolution into the temporal domain. See text for additional details.

In a second approach, a microsecond xenon flashlamp was used to generate narrow excitation pulses, and the rising edge of the pulse served as the trigger signal. The flashlamp was coupled into the microscope using a custom-built adapter that replaced the regular filter block. This adapter housed a dichroic mirror rotated 90° about the vertical axis with respect to the standard position; thus, the beam was introduced from the side, rather than the back, of the microscope. Quartz optical elements were used for 1) collimating the light, 2) suppressing infrared radiation, 3) selecting an appropriate excitation band, and 4) refocusing the beam onto the back focal planes of the microscope objectives. This approach minimized light losses from optical elements, of particular importance in the case of the UV illumination necessary to excite many lanthanide chelates.

Detection of luminescence images was with cooled slow-scan scientific CCD cameras. These were either used directly on the camera port of the microscope or, for time-resolved detection, placed behind a MCP intensifier. The gated photocathode of the intensifier was driven by a pulse/delay generator defining the time window of observation. The latter could be delayed precisely, relative to the start (or end) of the excitation pulse. The illumination systems provided excitation pulses at 100–200 Hz repetition rates synchronized to the boxcar detection. The luminescence derived from these cycles was integrated by the CCD camera during the exposure time.

The advantages of the microsecond flashlamp source are excellent time resolution (submicrosecond) and strong emission in the near UV. Thus, one can resort to the new probes with emission lifetimes in the microsecond range (Hennink et al., 1996; Li et al., 1997b; Szmacinski et al., 1996; Terpetschnig et al., 1995b, 1996; Youn et al., 1995) as well as the longer-lived lanthanide chelates. However, a mechanical chopper is simpler to install and is cost effective. Chopper wheels with different slit sizes and numbers can provide open and closed periods down to 200 μs. Such excitation pulses are efficient for many currently available probes, and even when using the longer (1-ms) excitation pulses with a duty cycle of 20%, one can still detect reasonable fluorescence from shorter-lived labels in the sample. This gains importance in measurements in which a long-lived chelate is used as energy transfer donor and a fluorophore with a lifetime in the nanosecond range as the acceptor. Under these conditions, the direct fluorescence of the latter can be observed visually and measured simply by switching the gating of the detection and changing the excitation filter, i.e., without major changes to the illumination pathway. In the case of the microsecond lamp, this is not possible, inasmuch as a pulse width of 2 μs and a repetition rate of 100 Hz yield a duty cycle of only 0.02%, hindering direct visual observation and necessitating extremely long exposure times.

The time-resolved images of the Eu crystals were of comparable luminosity using the 100-W Hg lamp with 1-ms open and 4-ms closed illumination intervals (200-Hz cycle) or the microsecond flashlamp operating at a 200-Hz repetition rate. Both of these two approaches yielded a nominal mean power of 20 W. The advantage of the microsecond flashlamp is that the energy of 5 ms of continuous illumination is packed into a microsecond pulse, making this device ideal for time-resolved microscopy in the micro- to millisecond range in contrast to nanosecond flashlamps that have a very low pulse energy.

For spectral resolution, a stigmatic imaging spectrograph was mounted on the second camera port of the microscope. The entrance slit of the spectrograph was positioned precisely at the primary image plane. An initial image of the field encompassed by the slit was recorded by operating the spectrograph at zero dispersion (0 nm) and opening the slit to 1–3 mm. After repositioning the microscope stage as desired, the slit was reduced (typically to 50 μm) and the monochromator drive activated so as to select the central wavelength of the spectral region. Images were collected using a cooled slow-scan CCD camera mounted on the exit aperture of the spectrograph. The rectangular images carried the spatial information from the stripe of sample projected onto the input slit along one (short) axis and spectrally resolved along the other (long) axis. For extending the resolution to the temporal domain, the MCP intensifier was installed on the output aperture of the spectrograph so that the spectral image impinged on the photocathode. The intensified image from the phosphor of the intensifier was then projected onto the CCD chip.

Detection of Eu-DTPA-cs124 crystals using chopped illumination

The chopper-based time-resolved system was tested and optimized using Eu-DTPA-cs124 crystals mounted under quartz coverslips. The MCP voltage was set to 800 V. The images shown in Fig. 3 were integrated for 5 s, with the photocathode open for 0.5 ms in each cycle. The delays after the cessation of illumination increased by 0.5 ms in images 1 (0-ms delay) through 7. The images were digitized with 12-bit resolution and converted to floating point in SCIL-Image. The intensity $I(x, y)$ at every pixel was mapped to $Q(x, y)$ according to

$$Q(x, y) = \log\{I(x, y) - B(x, y)\} - 1, \tag{4}$$

where $B(x, y)$ was the blank intensity at pixel (x, y) of the CCD using a similarly processed sample without crystals. The resulting $Q(x, y)$ values from all images were pooled to define the total range used for contrast stretching onto an 8-bit pseudocolor scale for display (Fig. 3). The last panel shows the decay of fluorescence after the cessation of illumination calculated from the mean intensities of the crystal labeled with 'a' in panel 1. The decay corresponded very well to a single exponential function ($r = 0.99963$), yielding a lifetime of 0.92 ms, in agreement with the value (0.9 ms) measured in a spectrofluorometer (Selvin et al., 1996).

Luminescence spectrum of Eu chelate crystals

Europium chelate crystals were imaged in full field mode with the slow-scan CCD camera (Fig. 4 *a*). The entrance slit

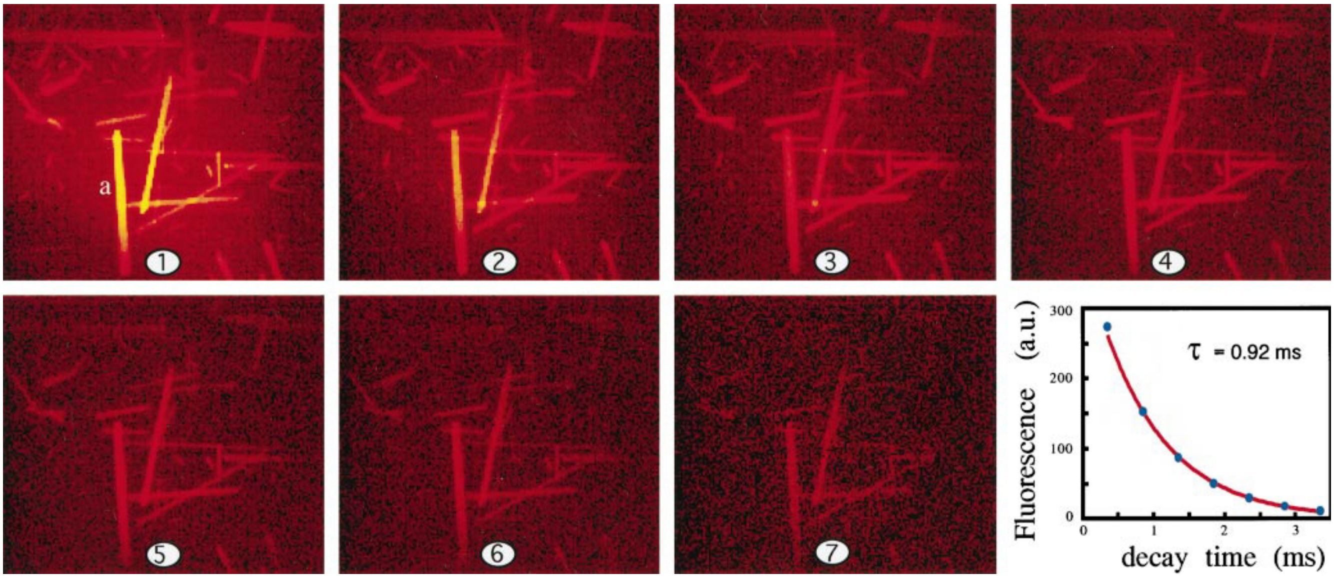

FIGURE 3 Time-resolved detection of Eu-DTPA-cs124 luminescence. Eu-DTPA-cs124 crystals were mounted under a quartz coverslip and observed through a 40× NA 0.6 Ultrafluar glycerol immersion objective, using a 340-nm bandpass excitation filter, a 390-nm dichroic mirror, and a 400-nm longpass emission filter. Illumination with the chopped Hg lamp beam was for 0.5 ms, and the emission was detected for an interval of 0.5 ms after delays of 0, 0.5, 1, 1.5, 2.0, 2.5, and 3 ms in images 1 through 7. A total of 1000 excitation-emission cycles were integrated on the CCD chip (5-s exposures). The resulting images are presented on a logarithmic pseudocolor scale. The intensity in the crystal marked with an 'a' was averaged and plotted in the last panel as a function of the delay time between the onset of excitation and detection of emission. The continuous curve represents the exponential fit to the data.

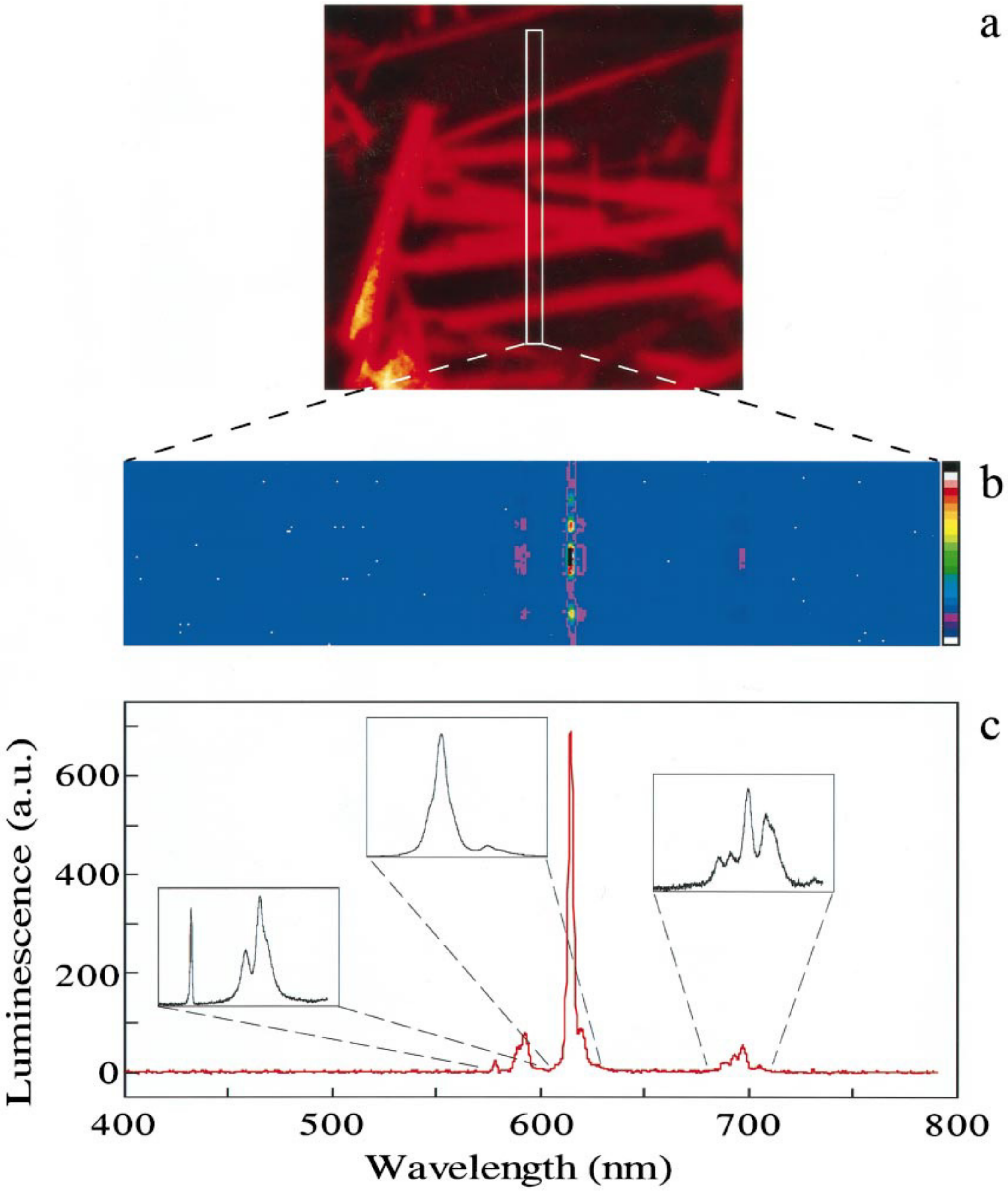

FIGURE 4 Emission spectra of Eu-DTPA-cs124 crystals. (*a*) Pseudocolor image of a field of view with several crystals observed through a 40× NA 0.6 Ultrafluar objective and 330-nm wide bandpass excitation, 400-nm dichroic, and 400-nm longpass emission filters. The projection of the entrance slit of spectrograph (50 μm) is outlined as a white rectangle. On the image formed by the spectrograph, the vertical dimension of the original image is retained, whereas the emission spectrum is formed along the horizontal axis. (*b*) Intensity values belonging to every vertical element of the image projected onto the slit and to various wavelengths are mapped to an arbitrary color scale displayed on the right side. (*c*) Emission spectrum extracted from data in *b*. The spectrum was taken with a 300 grooves/mm grating, using 3 × 2 binning on the CCD chip. The background correction was estimated from an area of the image devoid of crystals. Insets show high-resolution spectra of the characteristic Eu emission lines obtained with a 1200 grooves/mm grating and 1 × 2 binning on the chip. The wavelength scales in *b* and *c* are identical.

of the spectrograph was then adjusted to 100 μm; its image is overlaid in Fig. 4 *a* so as to indicate the stripe of the sample projected into the spectrograph. For obtaining high-resolution spectra, the slit was set to its minimum of 50 μm.

In the images produced by the spectrograph, the *y* (vertical) axis corresponds to the original spatial dimension, with the spectra dispersed along the orthogonal (horizontal) *x* axis (Fig. 4 *b*). Intensities are in arbitrary units and contrast stretched linearly according to the color bar on the right. The image was obtained with the 300 grooves/mm grating of the spectrograph in three exposures, using three different central wavelengths (450, 600, and 700 nm) and then spliced together. Spectra were extracted by vertically binning lines corresponding to either crystal-containing or

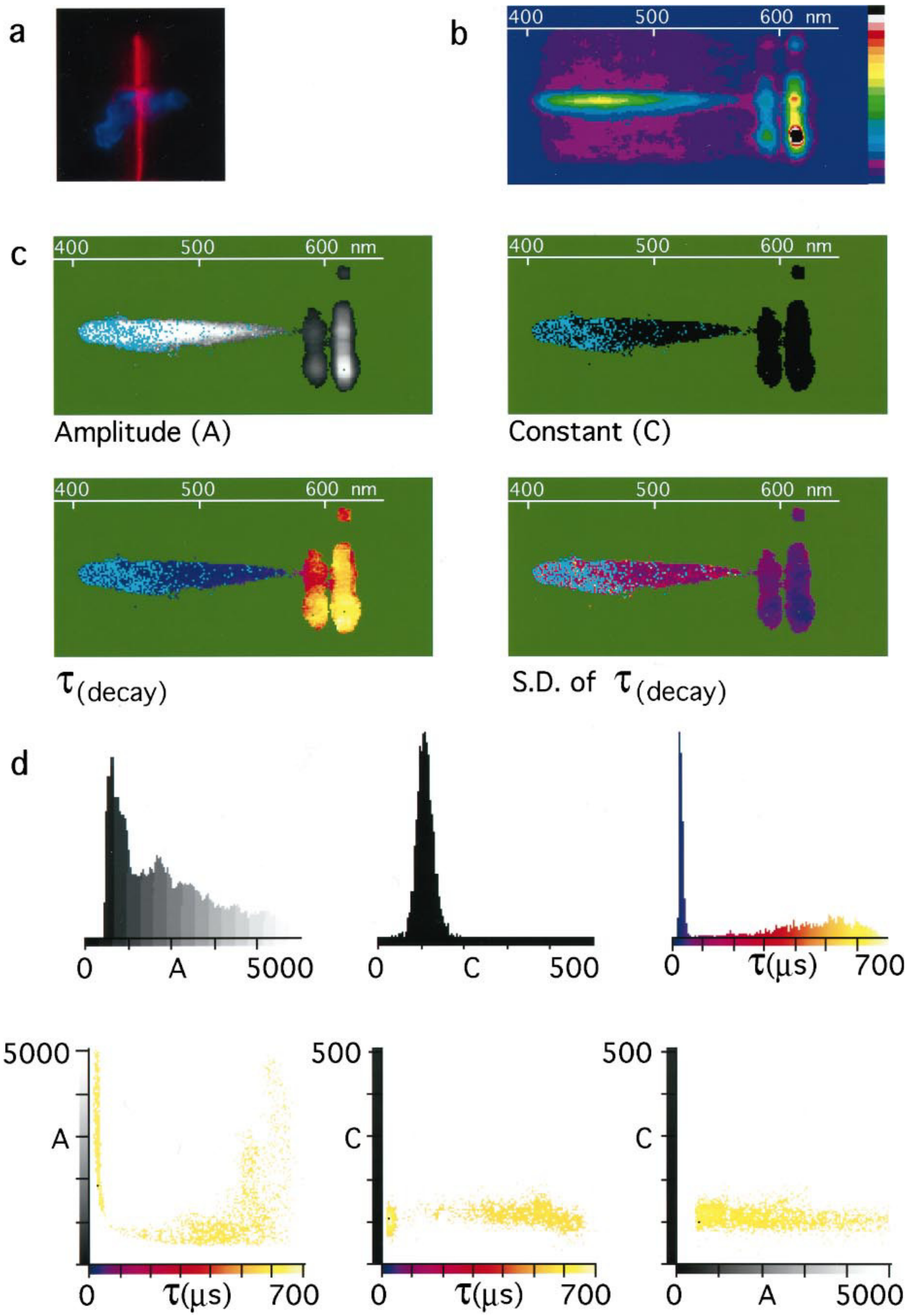

FIGURE 5 Spectral and temporal resolution in the microscope. For demonstrating the time- and spectrum-resolved imaging capabilities of the system, a Eu-DTPA-cs124 crystal positioned over a dried patch of DTPA-cs124 was chosen. (*a*) Pseudocolor fluorescence image, created by the overlay of 450-

background regions. The signals were averaged and background subtracted, producing the spectra shown in Fig. 4 *c*.

The resolution was nominally 0.68 nm per pixel (i.e., the 250 binned pixels of the CCD corresponded to 171 nm). Because of the relatively large (100-μm) entrance slit and 20 nm/mm linear dispersion of the grating, the calculated spectral bandwidth was 2 nm. The $^5D_0 \rightarrow {}^7F_0$ transition at 580 nm (see later) is inherently extremely sharp because it cannot be split by the crystal field. Thus, in practice, the observed linewidth of this transition is often determined by the actual spectrometer resolution. The FWHM of the 580-nm line was 2.7 nm. The somewhat lower than specified resolution probably reflected a failure of the output port of the microscope to fill the *f*/4 entrance aperture of the spectrograph.

The contribution of cs124 fluorescence in the 400- to 550-nm range (see also Fig. 5 *b*) was not significant because its emission is primarily below 420 nm and because chelation decreases the direct emission of cs124 approximately fivefold. The characteristic lines of europium were seen at 580, 590–595, 617–620, and 680–708 nm, corresponding to the $^5D_0 \rightarrow {}^7F_J$ transitions with $J = 0$, 1, 2, and 4, respectively (Carnall et al., 1968). The 650-nm line of the $^5D_0 \rightarrow {}^7F_3$ transition was extremely weak, although it could be seen upon expansion of the scale.

The insets of Fig. 4 *c* show high-resolution spectra derived from images taken with the 1200 grooves/mm holographic grating and recorded in the 1×2 binning mode of the CCD, corresponding to 0.051 nm per point and a total range of 38 nm. As the CCD pixel width was 23 μm, the actual resolution was defined by the 50-μm entrance slit, which with the 5 nm/mm dispersion grating would yield a 0.25-nm bandwidth. The FWHM of the 580-nm line was 0.46 nm, indicating that the aperture mismatch caused a slight degradation of resolution.

Potentially, each $^5D_0 \rightarrow {}^7F_J$ transition can be split by the Stark effect into $2J + 1$ (which equals m_J) different levels, although point symmetry about the lanthanide ion reduces this number, creating degeneracy between different m_J values. Pentagonal symmetry results in $J + 1$ splittings; this condition seemed to correspond to our data: all of the $J =$ 0, 1, 3, or 4 lines had $J + 1$ splittings, and the polarization data (see below) showed that the $J = 2$ component also followed this rule. The actual symmetry of our crystal is less than pentagonal (Selvin et al., 1996), but the shifts in energy levels may not be great enough to be resolved except for $J = 1$ (see polarization data).

Inasmuch as the emission lines of Eu are well separated from the excitation band of cs124, these chelates offer very good spectral discrimination of the specific signals from scattered excitation light when used as luminescent markers. Furthermore, they can be combined with most UV-excitable probes (e.g., the coumarin 7-amino-4-methylcoumarin-3-acetic acid) in multicolor imaging utilizing the same excitation wavelength. The narrow emission bands are useful in achieving a good signal relative to sample autofluorescence, which generally has a significantly broader emission spectrum. The lanthanide chelates coupled to an appropriate acceptor (e.g., the sulfoindocyanines Cy5 or Cy5.5) result in a favorably high value of the overlap integral defining the sensitivity of FRET. An additional benefit is the lack of significant cross-talk into the acceptor emission channel (Li and Selvin, 1995).

Spectrally and temporally resolved imaging of Eu chelate crystals

The orthogonal nature of the spectral and temporal information reflecting the photophysical properties of molecules acting as reporter probes provides the impetus for the combined implementation of these modalities in the digital imaging microscope. In Fig. 5, we demonstrate the capacity of our instrument for carrying out such measurements. Fig. 5 *a* depicts a particular area of a europium crystal sample, surrounded by a solution of free cs124. The image is an overlay of two separate exposures with the CCD, both using a wideband UV excitation and a 400-nm dichroic mirror. The first exposure (shown in red pseudocolor) was taken through a 620-nm bandpass filter, and the second exposure (shown in blue pseudocolor) was through a 450-nm bandpass filter. The sample was positioned such that the crystal was projected onto the entrance slit of the spectrograph (50 mm) with the diminutive cs124 spot localized slightly below the center of the image. The resulting spectral image is shown in Fig. 5 *b* in pseudocolor. The band at 400–570 nm originates from the cs124. The other two high-intensity regions just below and above 600 nm correspond in position to the chelate crystal and identify the emission as originating from $^5D_0 \rightarrow {}^7F_0$, $^7F_1$, $^7F_2$ transitions of Eu.

A sequence of time-resolved exposures was then obtained from this spectral image. The microsecond flashlamp was

and 620-nm emissions originating from the cs124 and the europium, respectively. The spectrograph slit was set to 50 μm and positioned vertically over the crystal so that a small spot of cs124 was also in view, a little below the center. Spectral images were taken with the microsecond flashlamp as the excitation source and the gated MCP intensifier fitted between the spectrograph and the CCD camera. The 300 grooves/mm grating was used at 520 nm central wavelength. (*b*) Spectrally resolved image at the outset of the decay process. The detection started simultaneously with the excitation flash, and the photocathode open time after each flash was 100 μs. The image was integrated for 5 s (500 cycles). Subsequently, a series of 37 images were taken under similar conditions, except the delay between the excitation flash and start of detection was 100 μs longer in every image of the sequence. The pseudocolor scale bar is linear. (*c*) Results of a single exponential fit was calculated for every pixel: distributions of (initial) luminescence amplitude (A), constant offset (C), the decay time constant (lifetime, τ), and the SD thereof. (*d*) Distribution histograms of amplitude, offset, and lifetime and the correlation of pairwise combinations of the parameters.

used for intermittent illumination. In all exposures, the cathode on-gated time of the MCP intensifier was 100 μs. The delays from the rising edge of the excitation pulse were multiples of 100 μs extending from 0 to 3.6 ms in 37 consecutive exposures. The sequence was imported into SCIL-Image, and the program DECAY was used to fit an exponential (plus offset) to every pixel. Fig. 5 *c* shows the result of the fit; the panels are histograms of the amplitude and constant (offset) and of the decay constant τ and its standard deviation (SD). Pixels below threshold are assigned a green color, whereas pixels for which the exponential fit did not meet certain criteria (Gadella and Jovin, 1997) are labeled blue. These pixels corresponded primarily to the fluorescence from the short-lived (nanosecond lifetime) cs124, which could not be resolved with the 100-μs boxcar window. Intensity values are represented on a gray scale, and τ and SD of τ are on a pseudocolor scale, the values of which are given in the histograms (Fig. 5 *d*).

The distribution of the decay time constant displayed two peaks, one ~12 μs and the other centered at ~650 μs. The former corresponded to the cs124 spot as judged from the two-dimensional τ map (Fig. 5 *d*). Inasmuch as the fluorescence lifetime of cs124 is in the nanosecond range, the apparent lifetime probably reflected the decay course of the excitation flash. By applying a shorter boxcar time window (5 μs) and a 5-μs increment, a sequence of images was obtained that yielded a decay time of the excitation light pulse of 7.9 ± 1.5 μs for the 300- to 380-nm UV range. According to the manufacturer's specification, the FWHM of the pulse is 300–450 ns, depending on the wavelength. The flash follows the preliminary discharge after 2 μs, and with the 110-nF capacitor and 1-kV potential difference used, it decays by a factor of 10^4 in 40 μs. In view of these specifications, a decay time of ~8 μs seems long. However, we determined that the decay occurred much faster during the first microsecond than in the tail, thus accounting for the long apparent decay time observed with the 5-μs interval. In accordance with this rationale, fitting the exponential starting only with the second 5-μs emission window after excitation led to a decay time of 17 ± 2 μs.

The other peak of the decay time histogram centered at 640 ± 117 μs corresponded to the lifetime of europium electronic transitions. The contribution of the tail of the flash could be eliminated by excluding the first image from the analysis. Using this strategy, and at the same time gating on the lanthanide emission wavelengths in the spectral domain, the exponential fit yielded a lifetime of 829 ± 83 μs. We also performed dual exponential fits on the whole temporal sequence (still gating on the lanthanide emission part of the spectrum), which led to 824 ± 126 μs for the long lifetime component, albeit with more pixels excluded from the analysis. This value was in excellent agreement with the lifetime of 0.92 ms found with chopped illumination.

The distribution of initial amplitudes also appeared to have several peaks, although not very well resolved. From its correlation with the lifetime (*A* versus τ diagram, Fig. 5 *d*), it is apparent that both the short-lived cs124 and long-lived europium luminescence exhibited the full range of initial amplitudes. In particular, a population of low-valued pixels had decay times intermediate between that of cs124 and the europium chelate. These pixels were located at the edges of the spectral peaks and thus were low in intensity, leading inevitably to less reliable fits.

Polarization properties of the Eu chelate crystals

Cuvette-based time-resolved luminescence (phosphorescence) anisotropy measurements have been used extensively in the past for assessing the rotational mobility of membrane proteins (Austin et al., 1979; Damjanovich et al., 1983; Jovin et al., 1982; Zidovetzki et al., 1991). A recent trend is the synthesis of long-lived probes that are suitable for studying the dynamics of other molecular motions, usually characterized by correlation times in the microsecond range (Lakowicz et al., 1995; Li et al., 1997a,b; Szmacinski et al., 1996; Terpetschnig et al., 1995a, 1996). Although it would be of great interest to perform such measurements in the microscope (especially in the case of adherent living cells), microscope-based polarization measurements have so far been restricted primarily to steady-state assays (Andreev et al., 1993; Mickols et al., 1985; Verkman et al., 1991). Another dimension of interest in the determination of polarization in the microscope is provided by spectral resolution. In the case of lanthanide chelates this feature is of particular importance, inasmuch as polarization measurements can distinguish between the magnetic and electric dipole nature of electronic transitions (Drexhage, 1970). As Förster-type singlet-singlet resonance energy transfer is based on dipole-dipole interaction (Förster, 1946), only the electric dipole lines of the lanthanide chelates should be taken into account when computing the overlap integral related to the FRET efficiency (Dexter, 1953). In addition, knowledge of the polarization properties of the chelate emission is essential for evaluating the orientation factor κ^2. If the ligand field polarizes the otherwise isotropic lanthanide emission, a value of ⅔ for κ^2 can no longer be assumed unless there is dynamic averaging by rotational reorientation of both donor and acceptor during the excitation state lifetime.

Owing to the long (millisecond) lifetime, lanthanide chelate molecules are likely to be rotationally depolarized in solution. However, microscopic crystals in which the chelate is immobilized such that the effects of rotational and lateral diffusion are excluded are well suited for anisotropy measurements. This can be performed in the microscope, as shown in Fig. 6. In Fig. 6 *a*, the full luminescence spectrum (solid line) is displayed together with the calculated polarization value P_h (Eq. 1, empty circles). Fig. 6, *b* and *c*, depicts high-resolution spectra and the polarization values obtained from an Eu-DTPA-cs124 crystal as defined in Eqs. 1 and 2, i.e., using different positions of the excitation polarizer and the emission analyzer. The background-subtracted average spectra were used to calculate P_h (Eq. 1,

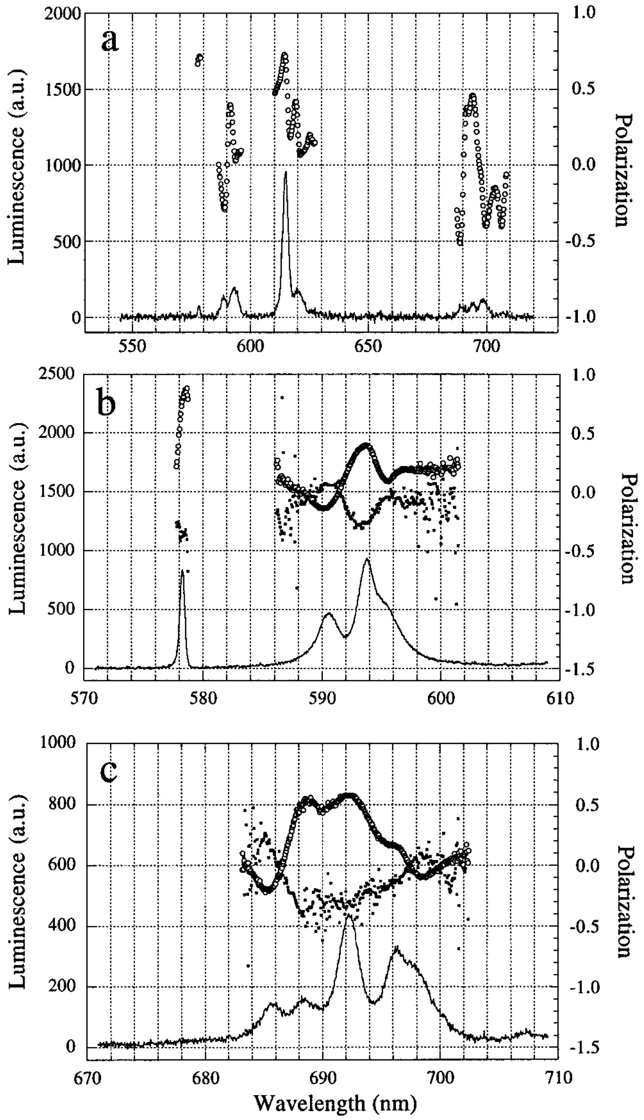

FIGURE 6 Polarization properties of europium chelate crystals. Polarized spectra from a Eu-DTPA-cs124 crystal were collected using continuous illumination as described in the legend to Fig. 4. A polarizer was inserted into the excitation path before the bandpass filter, and the analyzer was placed between the emission filter and the tube lens. Spectra taken with a 50-μm slit width and 1 × 2 binning on the CCD for all four combinations of polarizer/analyzer positions: (*a*) 300 grooves/mm grating, 630-nm center wavelength; (*b*) 1200 grooves/mm grating, 590-nm center wavelength; (*c*) 1200 grooves/mm grating, 690-nm center wavelength. P_h (○) and P_v (■) were calculated according to Eqs. 1 and 2 in Materials and Methods. Polarization values are plotted only for wavelength regions with intensities significantly above background. The spectral dependence of the correction factors G_h and G_v was determined according to Eq. 3 from a 0.1 mM solution of the same chelate. For reference, the luminescence spectrum is presented in each panel (——).

empty circles) and P_v (Eq. 2, closed squares), which have been plotted only at wavelengths corresponding to luminescence significantly above background levels. The P_v curves are more scattered as, owing to the excitation polarization perpendicular to the crystal axis, the emission intensities were weaker than in the case of P_h. The polarization spectra derived from independent data sets were reproducible. Rotating the excitation polarizer from horizontal to vertical (P_h curves versus P_v curves in Fig. 6, *b* and *c*) or the crystal (data not shown) by 90° led to an inversion of the observed polarization patterns. This implies that the correction factors G_h and G_v were determined correctly and that there was no residual bias in the instrumentation.

The most general conclusion from the polarization data is that europium is indeed polarized, at least in a crystal. It has often been assumed that lanthanide emission is unpolarized because of the high-spin to high-spin origin of the emission and the spherical symmetry of the isolated atom. In fact, the observed polarization spectra are consistent with an emission arising from electric (or magnetic) dipole transitions, as has been previously shown in europium chelates in thin films (Drexhage, 1970). Such transitions, denoted as forced dipole transitions, are allowed, despite the parity-forbidden nature of the transitions (4f → 4f electronic transitions) because of a small admixture of odd-parity (5d) states. Each Stark sublevel of a $^5D_0 \rightarrow {}^7F_J$ group will have different polarization depending on the particular m_J value, the extent of degeneracy of different m_J values, their relative contributions to the luminescence, and whether the transition is a magnetic or an electric dipole.

Specifically, the $^5D_0 \rightarrow {}^7F_0$ must have $m_J = 0$, and hence its polarization is oriented along the symmetry-breaking direction of the crystal field. For the $^5D_0 \rightarrow {}^7F_1$ transitions at 590–95 nm, polarization measurements help resolve the doublet seen in intensity measurements (Fig. 4 *c*) into a triplet (Fig. 6 *b*). The $^5D_0 \rightarrow {}^7F_1$ transitions are believed to arise from magnetic dipole transitions (Bunzli, 1989; Drexhage, 1970), which would yield three emission lines with polarization perpendicular to that of the electric dipole transition spanning the same energy level. We cannot as yet assign m_J values to each line in the triplet; thus, it is not possible to deduce the relative orientation of the $^5D_0 \rightarrow {}^7F_1$ magnetic dipole to the $^5D_0 \rightarrow {}^7F_0$ electric dipole(s). It is also conceivable that some of the lines are of mixed electric/magnetic dipole nature.

The main $^5D_0 \rightarrow {}^7F_2$ group was well resolved into three distinct polarization levels (Fig. 6 *a*) corresponding to a pentagonal crystal symmetry. The polarization was large (parallel to the direction of the $^5D_0 \rightarrow {}^7F_0$ transition), even though the m_J values are partially overlapped (see also the two peaks in Fig. 4 *c*). Consequently, for this group, the contribution to luminescence must have been primarily from the $m_J = 0$ transition.

The $^5D_0 \rightarrow {}^7F_4$ transition (680–708 nm) had five principal lines, which were distinguishable by polarization (Fig. 6 *c*). Because the maximal number of lines is nine, each of the five lines must have comprised more than one m_J value. However, the width of each of the five lines was wider than the spectral resolution of the instrument, and hence the degeneracy of the different m_J values in each line was not complete. Such degeneracy, even if not complete, would tend to reduce the polarization of each principal line.

The fact that europium emission is polarized has potentially practical ramifications. If the europium can be fixed rigidly to a macromolecule, then polarization anisotropy measurements on a time scale much longer than nanosecond fluorescence depolarization may be possible. These results also imply that one should not automatically assume that europium acts as an unpolarized donor in resonance energy transfer, particularly when using the $^5D_0$–$^7F_2$ emission lines to transfer to an acceptor. On the other hand, if one uses the $^5D_0$–$^7F_4$ lines, the net polarization will be smaller, depending on the symmetry of the ligand field around the lanthanide. In addition, it is anticipated that in solution the emission from all lines would be depolarized.

Concluding remarks

The incorporation of dual spectral and temporal resolution modes in the microscope, complemented by digital image processing gated on the spatial, spectral, and temporal dimensions results in a flexible and versatile analytical tool for microsamples and cytochemical specimens. We have described various configurations of a fluorescence microscope with which spectral and microsecond temporal resolution can be implemented in combination with conventional digital imaging based on CCD cameras

One of the two illumination methods presented here for time-resolved imaging is based on a chopped continuous light source and is relatively easy to implement. The other incorporates a new microsecond xenon flashlamp, which is comparable in power but has the advantage of delivering strong excitation pulses in short times. This makes it ideal for the application of recently developed fluorophores with lifetimes in the submicrosecond to microsecond range (Hennink et al., 1996; Li et al., 1997b; Terpetschnig et al., 1995b; Verwoerd et al., 1994; Youn et al., 1995). These offer a higher frequency of activation-emission (higher duty cycle), i.e., better luminosity.

In this report, we characterized a newly developed lanthanide chelate, the Eu-DTPA-cs124 (Li and Selvin, 1995, 1997; Selvin et al., 1996). This and related compounds are not only good potential labels for time-resolved imaging microscopy (Dahlen et al., 1994; de Haas et al., 1996; Seveus et al., 1992) but are also candidates for FRET measurements in the microscope used to estimate molecular proximity (Förster, 1946; Jovin and Arndt-Jovin, 1989; Selvin, 1995; Selvin and Hearst, 1994; Szöllösi et al., 1984). Although there are examples of LRET determinations using long-lived fluorophores in cuvette (Mathis, 1995; Selvin and Hearst, 1994; Selvin et al., 1994; Youn et al., 1995), no microscope-based applications have been reported to date. The millisecond lifetime and sharp line spectrum of the chelate tested, as well as the fairly large (5.6-nm) critical transfer distance R_0 value when used in combination with the sulfoindocyanine dye Cy5 as an acceptor, make it an ideal LRET donor (Li and Selvin, 1995; Selvin et al., 1996). The application of dual temporal and spectral discrimination in our microscope exploits these features extremely well. For example, it should be possible to acquire images of sensitized acceptor emission, excluding direct acceptor emission by temporal gating and donor emission by spectral gating. One could also calculate LRET from the change in the acceptor emission spectrum and polarization in the presence of the donor (Clegg, 1996). The acquisition of spectrally resolved polarization data can also be of great utility for the evaluation of the orientation factor κ^2.

G. Vereb was the recipient of a postdoctoral fellowship from the Alexander von Humboldt Foundation and supported by Hungarian National Research Fund grants OTKA F013335 and F025210. P.R. Selvin was supported by National Institutes of Health grant AR44420.

REFERENCES

Altamirano-Bustamante, A., G. Barnard, and F. Kohen. 1991. Direct time-resolved fluorescence immunoassay for serum oestradiol based on the idiotypic anti-idiotypic approach. *J. Immunol. Methods*. 138:95–101.

Andreev, O. A., A. L. Andreeva, and J. Borejdo. 1993. Polarization of fluorescently labeled myosin subfragment-1 fully or partially decorating muscle fibers and myofibrils. *Biophys. J.* 65:1027–1038.

Austin, R. H., S. S. Chan, and T. M. Jovin. 1979. Rotational diffusion of cell surface components by time-resolved phosphorescence anisotropy. *Proc. Natl. Acad. Sci. U.S.A.* 76:5650–5654.

Barnard, G., F. Kohen, H. Mikola, and T. Lovgren. 1989. The development of non-separation time-resolved fluoroimmunoassays for the measurement of urinary metabolites. *J. Biolum. Chemilum.* 4:177–184.

Beverloo, H. B., A. van Schadewijk, J. Bonnet, R. van der Geest, R. Runia, N. P. Verwoerd, J. Vrolijk, J. S. Ploem, and H. J. Tanke. 1992. Preparation and microscopic visualization of multicolor luminescent immunophosphors. *Cytometry*. 13:561–570.

Bunzli, J.-C. G. 1989. Luminescent probes. *In* Lanthanide Probes in Life, Chemical and Earth Sciences: Theory and Practice. J.-C. G. Bunzli and G. R. Choppin, Eds. Elsevier, New York, 219–293.

Burroughs, S. E., W. D. Horrocks, Jr., H. Ren, and C. B. Klee. 1994. Characterization of the lanthanide ion-binding properties of calcineurin-B using laser-induced luminescence spectroscopy. *Biochemistry*. 33:10428–10436.

Carnall, W. T., P. R. Fields, and K. Rajnak. 1968. Spectral intensities of the trivalent lanthanides and actinides in solution. II. Pm^{3+}, Sm^{3+}, Eu^{3+}, Gd^{3+}, Tb^{3+}, Dy^{3+}, and Ho^{3+}. *J. Chem. Phys.* 49:4412–4423.

Churchich, J. E. 1995. Binding of a fluorescent nucleotide analog to Hsc70: the effect of peptide protein interactions on the luminescence properties of the probe. *Eur. J. Biochem.* 231:736–741.

Ci, Y. X., X. D. Yang, and W. B. Chang. 1995. Fluorescence labelling with europium chelate of beta-diketones and application in time-resolved fluoroimmunoassays (Tr-Fia). *J. Immunol. Methods*. 179:233–241.

Clark, I. D., J. P. MacManus, D. Banville, and A. G. Szabo. 1993. A study of sensitized lanthanide luminescence in an engineered calcium-binding protein. *Anal. Biochem.* 210:1–6.

Clegg, R. M. 1996. Fluorescence resonance energy transfer (FRET). *In* Fluorescence Imaging Spectroscopy and Microscopy. X. F. Wang and B. Herman, Eds. John Wiley & Sons, New York, 179–252.

Clegg, R. M., T. W. J. Gadella, Jr., and T. M. Jovin. 1994. Lifetime-resolved fluorescence imaging. *Proc. SPIE.* 2137:105–118.

Dahlen, P., L. Liukkonen, M. Kwiatkowski, P. Hurskainen, A. Iitia, H. Siitari, J. Ylikoski, V. M. Mukkala, and T. Lovgren. 1994. Europium-labeled oligonucleotide hybridization probes: preparation and properties. *Bioconjugate Chem.* 5:268–272.

Damjanovich, S., L. Tron, J. Szollosi, R. Zidovetzki, W. L. Vaz, F. Regateiro, D. J. Arndt-Jovin, and T. M. Jovin. 1983. Distribution and mobility of murine histocompatibility H-2Kk antigen in the cytoplasmic membrane. *Proc. Natl. Acad. Sci. U.S.A.* 80:5985–5989.

de Haas, R. R., N. P. Verwoerd, M. P. van der Corput, R. P. van Gijlswijk, H. Siitari, and H. J. Tanke. 1996. The use of peroxidase-mediated deposition of biotin-tyramide in combination with time-resolved fluorescence imaging of europium chelate label in immunohistochemistry and in situ hybridization. *J. Histochem. Cytochem.* 44:1091–1099.

Dexter, D. L. 1953. A theory of sensitized luminescence in solids. *J. Chem. Phys.* 21:836–850.

Dickson, E. F., A. Pollak, and E. P. Diamandis. 1995. Time-resolved detection of lanthanide luminescence for ultrasensitive bioanalytical assays. *J. Photochem. Photobiol*. 27:3–19.

Dix, J. A., and A. S. Verkman. 1990. Mapping of fluorescence anisotropy in living cells by ratio imaging: application to cytoplasmic viscosity. *Biophys. J.* 57:231–240.

Drexhage, K. H. 1970. Monomolecular layers and light. *Sci. Am.* 222: 108–119.

Förster, T. 1946. Energiewanderung und Fluoreszenz. *Naturwissenschaften*. 6:166–175.

Gadella, T. W. J., Jr., R. M. Clegg, and T. M. Jovin. 1994. Fluorescence lifetime imaging microscopy: pixel-by-pixel analysis of phase-modulation data. *Bioimaging*. 2:139–159.

Gadella, T. W. J., Jr., and T. M. Jovin. 1995. Oligomerization of epidermal growth factor receptors on A431 cells studied by time-resolved fluorescence imaging microscopy: a stereochemical model for tyrosine kinase receptor activation. *J. Cell Biol.* 129:1543–1558.

Gadella, T. W. J., Jr., and T. M. Jovin. 1997. Fast algorithms for the analysis of single and double exponential decay curves with a background term: application to time- resolved imaging microscopy. *Bioimaging*. 5:19–39.

Gadella, T. W. J., Jr., T. M. Jovin, and R. M. Clegg. 1993. Fluorescence lifetime imaging microscopy (FLIM): spatial resolution of microstructures on the nanosecond time scale. *Biophys. Chem.* 48:221–239.

Hennink, E. J., R. de Haas, N. P. Verwoerd, and H. J. Tanke. 1996. Evaluation of a time-resolved fluorescence microscope using a phosphorescent Pt-porphine model system. *Cytometry*. 24:312–320.

Heyduk, E., and T. Heyduk. 1997. Thiol-reactive luminescent Europium chelates: luminescence probes for resonance energy transfer distance measurements in biomolecules. *Anal. Biochem.* 248:216–227.

Joshi, N. B., and A. E. Shamboo. 1988. Distances between functional sites in cardiac sarcoplasmic reticulum (Ca^{2+} + Mg^{2+})-ATPase: inter-lanthanide energy transfer. *Eur. J. Biochem.* 178:483–487.

Jovin, T. M., and D. J. Arndt-Jovin. 1989. FRET microscopy: digital imaging of fluorescence resonance energy transfer. Application in cell biology. *In* Cell Structure and Function by Microspectrofluometry. E. Kohen, J. G. Hirschberg, and J. S. Ploem, Eds. Academic Press, London, 99–117.

Jovin, T. M., D. J. Arndt-Jovin, G. Marriott, R. M. Clegg, M. Robert-Nicoud, and T. Schormann. 1990. Distance, wavelength and time: the versatile 3rd dimensions in light emission microscopy. *In* Optical Microscopy for Biology. B. Herman and K. Jacobson, Eds. Wiley-Liss, New York, 575–602.

Jovin, T. M., M. Bartholdi, W. L. Vaz, and R. H. Austin. 1982. Rotational diffusion of biological macromolecules by time-resolved delayed luminescence (phosphorescence, fluorescence) anisotropy. *Ann. N.Y. Acad. Sci.* 366:176–196.

Konig, K., P. T. So, W. W. Mantulin, B. J. Tromberg, and E. Gratton. 1996. Two-photon excited lifetime imaging of autofluorescence in cells during UVA and NIR photostress. *J. Microsc.* 183:197–204.

Kwiatkowski, M., M. Samiotaki, U. Lamminmaki, V. M. Mukkala, and U. Landegren. 1994. Solid-phase synthesis of chelate-labelled oligonucleotides: application in triple-color ligase-mediated gene analysis. *Nucleic Acids Res.* 22:2604–2611.

Kwok, F., and J. E. Churchich. 1994. The binding of substrates and inhibitors to the metal center of myoinositol monophosphatase. *FEBS Lett.* 346:304–306.

Lakowicz, J. R., H. Malak, I. Gryczynski, F. N. Castellano, and G. J. Meyer. 1995. DNA dynamics observed with long lifetime metal-ligand complexes. *Biospectroscopy*. 1:163–168.

Lakowicz, J. R., H. Szmacinski, K. Nowaczyk, W. J. Lederer, M. S. Kirby, and M. L. Johnson. 1994. Fluorescence lifetime imaging of intracellular calcium in COS cells using Quin-2. *Cell Calcium*. 15:7–27.

Li, M., and P. R. Selvin. 1995. Luminescent polyaminocarboxylate chelates of terbium and europium: the effect of chelate structure. *J. Am. Chem. Soc.* 117:8132–8138.

Li, M., and P. R. Selvin. 1997. Amine-reactive forms of a luminescent diethylenetriaminepentaacetic acid chelate of terbium and europium: attachment to DNA and energy transfer measurements. *Bioconjugate Chem*. 8:127–132.

Li, L., H. Szmacinski, and J. R. Lakowicz. 1997a. Long-lifetime lipid probe containing a luminescent metal-ligand complex. *Biospectroscopy*. 3:155–159.

Li, L., H. Szmacinski, and J. R. Lakowicz. 1997b. Synthesis and luminescence spectral characterization of long-lifetime lipid metal-ligand probes. *Anal. Biochem.* 244:80–85.

Marriott, G., R. M. Clegg, D. J. Arndt-Jovin, and T. M. Jovin. 1991. Time resolved imaging microscopy: phosphorescence and delayed fluorescence imaging. *Biophys. J.* 60:1374–1387.

Marriott, G., M. Heidecker, E. P. Diamandis, and Y. Yan-Marriott. 1994. Time-resolved delayed luminescence image microscopy using an europium ion chelate complex. *Biophys. J.* 67:957–965.

Martini, J. L., C. Tetreau, F. Pochon, H. Tourbez, J. M. Lentz, and D. Lavalette. 1993. On the mechanism of energy transfer to Tb^{3+} ions in proteins: a time-resolved luminescence study of the Tb-elastase complex. *Eur. J. Biochem.* 211:467–473.

Mathis, G. 1995. Probing molecular interactions with homogeneous techniques based on rare earth cryptates and fluorescence energy transfer. *Clin. Chem*. 41:1391–1397.

Mickols, W., M. F. Maestre, I. Tinoco, Jr., and S. H. Embury. 1985. Visualization of oriented hemoglobin S in individual erythrocytes by differential extinction of polarized light. *Proc. Natl. Acad. Sci. U.S.A.* 82:6527–6531.

Root, D. D. 1997. *In situ* molecular association of dystrophin with actin revealed by sensitized emission immuno-resonance energy transfer. *Proc. Natl. Acad. Sci. USA*. 94:5685–5690.

Selvin, P. R. 1995. Fluorescence resonance energy transfer. *Methods Enzymol.* 246:300–334.

Selvin, P. R. 1996. Lanthanide-based resonance energy transfer. *IEEE JSTQE: Lasers Biol.* 2:1077–1087.

Selvin, P. R., and J. E. Hearst. 1994. Luminescence energy transfer using a terbium chelate: improvements on fluorescence energy transfer. *Proc. Natl. Acad. Sci. U.S.A.* 91:10024–10028.

Selvin, P. R., J. Jancarik, M. Li, and L. W. Hung. 1996. Crystal structure and spectroscopic characterization of a luminescent europium chelate. *Inorg. Chem.* 35:700–705.

Selvin, P. R., T. M. Rana, and J. E. Hearst. 1994. Luminescence resonance energy transfer. *J. Am. Chem. Soc.* 116:6029–6030.

Seveus, L., M. Vaisala, S. Syrjanen, M. Sandberg, A. Kuusisto, R. Harju, J. Salo, I. Hemmila, H. Kojola, and E. Soini. 1992. Time-resolved fluorescence imaging of europium chelate label in immunohistochemistry and in situ hybridization. *Cytometry*. 13:329–338.

Szmacinski, H., E. Terpetschnig, and J. R. Lakowicz. 1996. Synthesis and evaluation of Ru-complexes as anisotropy probes for protein hydrodynamics and immunoassays of high-molecular-weight antigens. *Biophys. Chem.* 62:109–120.

Szöllösi, J., L. Tron, S. Damjanovich, S. H. Helliwell, D. Arndt-Jovin, and T. M. Jovin. 1984. Fluorescence energy transfer measurements on cell surfaces: a critical comparison of steady-state fluorimetric and flow cytometric methods. *Cytometry*. 5:210–216.

Terpetschnig, E., H. Szmacinski, and J. R. Lakowicz. 1995a. Fluorescence polarization immunoassay of a high-molecular-weight antigen based on a long-lifetime Ru-ligand complex. *Anal. Biochem.* 227:140–147.

Terpetschnig, E., H. Szmacinski, and J. R. Lakowicz. 1996. Fluorescence polarization immunoassay of a high-molecular-weight antigen using a long wavelength-absorbing and laser diode-excitable metal-ligand complex. *Anal. Biochem.* 240:54–59.

Terpetschnig, E., H. Szmacinski, H. Malak, and J. R. Lakowicz. 1995b. Metal-ligand complexes as a new class of long-lived fluorophores for protein hydrodynamics. *Biophys. J.* 68:342–350.

Verkman, A. S., M. Armijo, and K. Fushimi. 1991. Construction and evaluation of a frequency-domain epifluorescence microscope for lifetime and anisotropy decay measurements in subcellular domains. *Biophys. Chem.* 40:117–125.

Verwoerd, N. P., E. J. Hennink, J. Bonnet, C. R. Van der Geest, and H. J. Tanke. 1994. Use of ferro-electric liquid crystal shutters for time-resolved fluorescence microscopy. *Cytometry*. 16:113–117.

Walters, J. D., and J. D. Johnson. 1990. Terbium as a luminescent probe of metal-binding sites in protein kinase C. *J. Biol. Chem.* 265:4223–4226.

Youn, H. J., E. Terpetschnig, H. Szmacinski, and J. R. Lakowicz. 1995. Fluorescence energy transfer immunoassay based on a long-lifetime luminescent metal-ligand complex. *Anal. Biochem.* 232:24–30.

Zidovetzki, R., D. A. Johnson, D. J. Arndt-Jovin, and T. M. Jovin. 1991. Rotational mobility of high-affinity epidermal growth factor receptors on the surface of living A431 cells. *Biochemistry*. 30:6162–6166.